© 2019. Published by The Company of Biologists Ltd | Development (2019) 146, dev177790. doi:10.1242/dev.177790

RESEARCH ARTICLE

The fenestrae-associated protein Plvap regulates the rate of blood-borne protein passage into the hypophysis

Ludmila Gordon[1], Janna Blechman[1], Eyal Shimoni[2], Dvir Gur[1], Bela Anand-Apte[3] and Gil Levkowitz[1,*]

ABSTRACT

To maintain body homeostasis, endocrine systems must detect and integrate blood-borne peripheral signals. This is mediated by fenestrae, specialized permeable pores in the endothelial membrane. Plasmalemma vesicle-associated protein (Plvap) is located in the fenestral diaphragm and is thought to play a role in the passage of proteins through the fenestrae. However, this suggested function has yet to be demonstrated directly. We studied the development of fenestrated capillaries in the hypophysis, a major neuroendocrine interface between the blood and brain. Using a transgenic biosensor to visualize the vascular excretion of the genetically tagged plasma protein DBP-EGFP, we show that the developmental acquisition of vascular permeability coincides with differential expression of zebrafish *plvap* orthologs in the hypophysis versus brain. Ultrastructural analysis revealed that *plvapb* mutants display deficiencies in fenestral diaphragms and increased density of hypophyseal fenestrae. Measurements of DBP-EGFP extravasation in *plvapb* mutants provided direct proof that Plvap limits the rate of blood-borne protein passage through fenestrated endothelia. We present the regulatory role of Plvap in the development of blood-borne protein detection machinery at a neuroendocrine interface through which hormones are released to the general circulation.

KEY WORDS: Fenestrae, PV-1, PV1, Hypothalamus, Pituitary, Neurohypophysis, Neuroendocrine, Vascular permeability, Blood-brain barrier, Zebrafish, Homeostasis, Circumventricular organs

INTRODUCTION

Endocrine organs regulate homeostasis by interfacing with blood vessels to enable the bidirectional passage of peptide hormones and blood-borne molecules to and from the general circulation. The capillaries of all endocrine organs contain fenestrae, which are circular membranal openings that cut through the cell body of endothelial cells. Fenestrae play a principal role in endocrine regulation of homeostasis by being more permeable to small and medium-sized molecules. Fenestrated capillaries are usually found in organs with rapid solute exchange, such as endocrine glands, gastrointestinal tract mucosa and kidney peritubular capillaries (reviewed by Aird, 2007; Stan, 2007). There are three major types of fenestrae: diaphragmed, non-diaphragmed and sinusoidal.

The diaphragmed fenestrae are pores, typically of 60-70 nm in diameter, that are traversed by a thin diaphragm (Rhodin, 1962). The only known molecular component associated with the fenestrae diaphragm is the type II transmembrane glycoprotein, which is encoded by the vertebrate plasmalemma vesicle-associated protein (*Plvap*) gene (Stan et al., 1999). Fenestral diaphragms consist of PLVAP homodimers, the C termini of which form the central density of the diaphragm (reviewed by Stan et al., 1999). In addition to its presence in the diaphragms of endothelial fenestrae, PLVAP is also localized in stomatal diaphragms of caveolae, as well as in transendothelial channels and endothelial pockets (Hamilton et al., 2019; Milici et al., 1986; Stan, 2005; Stan et al., 1999, 2004). Caveolae, which are subcellular pits of the plasma membrane of regular shape and size (50-100 nm), are found in endothelial and other cell types, and are known to be involved in transcytosis (reviewed by Filippini et al., 2018; Stan, 2005).

Several independent studies of *Plvap*-deficient mice have shown that PLVAP protein is required for diaphragm formation; however, it is not required for the formation of fenestral or caveolar pores (Herrnberger et al., 2012; Stan et al., 2012). The impairment of fenestral diaphragms has led to impaired barrier function of fenestrated capillaries, causing a disruption of blood composition, i.e. hypoproteinemia and hypertriglyceridemia. This led to early death of animals due to severe non-inflammatory protein-losing enteropathy, which is caused by uncontrolled plasma protein leakage (Herrnberger et al., 2012; Stan et al., 2012). It was suggested that PLVAP limits the passage of proteins through the fenestral pore; however, thus far there has been no direct demonstration of this suggested function.

The hypothalamo-hypophyseal system, which consists of the median eminence and neurohypophysis, is a major neuroendocrine interface, which allows the brain to regulate homeostasis by recognizing blood-borne proteins and releasing neurohormones into the general circulation (Anbalagan et al., 2018; Gutnick et al., 2011; Wircer et al., 2016). These two brain interfaces are also known as circumventricular organs (CVO), which are specialized areas located around the midlines of the brain ventricles (Ganong, 2000; Miyata, 2015). In contrast to CNS vasculature, which contains blood-brain barrier (BBB), capillaries of the CVO are fenestrated and, as such, they facilitate the bidirectional exchange of information between the CNS and the periphery without disrupting the BBB (Ciofi et al., 2009; Ganong, 2000; Miyata, 2015; Schaeffer et al., 2014). The role of PLVAP in CVO permeability, including that of the hypophysis, has never been studied before.

Here, we have investigated the necessity of Plvap in the developmental acquisition of permeability in the fenestrated capillaries of the zebrafish hypophysis. We found that the expression of two zebrafish PLVAP orthologs during development coincides with the acquisition of hypophyseal permeability to plasma proteins and the establishment of a permeability boundary between the hypophysis and BBB-containing vasculature.

---

[1]Department of Molecular Cell Biology, Weizmann Institute of Science, PO Box 26, Rehovot 7610001, Israel. [2]Chemical Research Support, Weizmann Institute of Science, PO Box 26, Rehovot 7610001, Israel. [3]Department of Ophthalmic Research, Cole Eye Institute, Cleveland Clinic Foundation, Cleveland OH 444195, USA.

*Author for correspondence (gil.levkowitz@weizmann.ac.il)

L.G., 0000-0003-4525-0786; D.G., 0000-0002-9140-1621; G.L., 0000-0002-3896-1881

Received 8 March 2019; Accepted 8 November 2019

We employed live imaging of zebrafish larvae to determine the dynamics by which a genetically labeled plasma protein passes through hypophyseal endothelia. Finally, we provide the first direct proof that PLVAP regulates the rate of blood-borne protein transfer through fenestrated endothelia into the hypophysis.

RESULTS

Hypophyseal vasculature is permeable to blood-borne proteins and lack BBB

To study the regulation of blood-borne protein passage through the hypophyseal blood capillaries, we used the zebrafish as a model system. Unlike in mammals, in which the hypothalamo-hypophyseal system is segregated into median eminence and neurohypophysis, the zebrafish hypophyseal vasculature consists of two adjoined neurovascular interfaces, the rostral and caudal pars nervosa, that originate from a hypophyseal vascular loop-like structure (Anbalagan et al., 2018; Gutnick et al., 2011; Liu et al., 2013). Hypophyseal capillaries of zebrafish larvae have a small diameter and they might be ruptured when using standard micro-angiography owing to increased blood volume. Therefore, we employed a non-invasive vascular permeability reporter, Tg(*l-fabp*:DBP-EGFP;*kdrl*:mCherry-caax) (Xie et al., 2010), that we have recently used to demonstrate hypophyseal permeability at 5 days post-fertilization (dpf) (Anbalagan et al., 2018). This double transgenic permeability reporter expresses the vitamin D-binding plasma protein fused to EGFP (DBP-EGFP) and a membrane-tethered mCherry reporter in endothelia, allowing simultaneous visualization of vascular morphology and DBP-EGFP extravasation from the blood into the parenchyma (Fig. 1A).

First, we visualized the extravasation of DBP-EGFP in the developing hypophyseal vasculature as well as in the adjacent brain vasculature (Fig. 1B-F). As we reported previously (Gutnick et al., 2011), the formation of a simple hypophyseal vascular loop-like structure is initiated at 3 dpf. At this embryonic stage, we detected faint but consistent DBP-EGFP signal inside the hypophyseal loop, as well as outside the hypophyseal artery and brain vasculature (Fig. 1B). At 5 dpf, a more pronounced extravasated DBP-EGFP signal was detected in the whole hypophyseal circumference in and around the hypophyseal capillary loop. At this post-embryonic larval stage, a permeability boundary started to form between the hypophyseal loop and the inferior hypophyseal artery, which

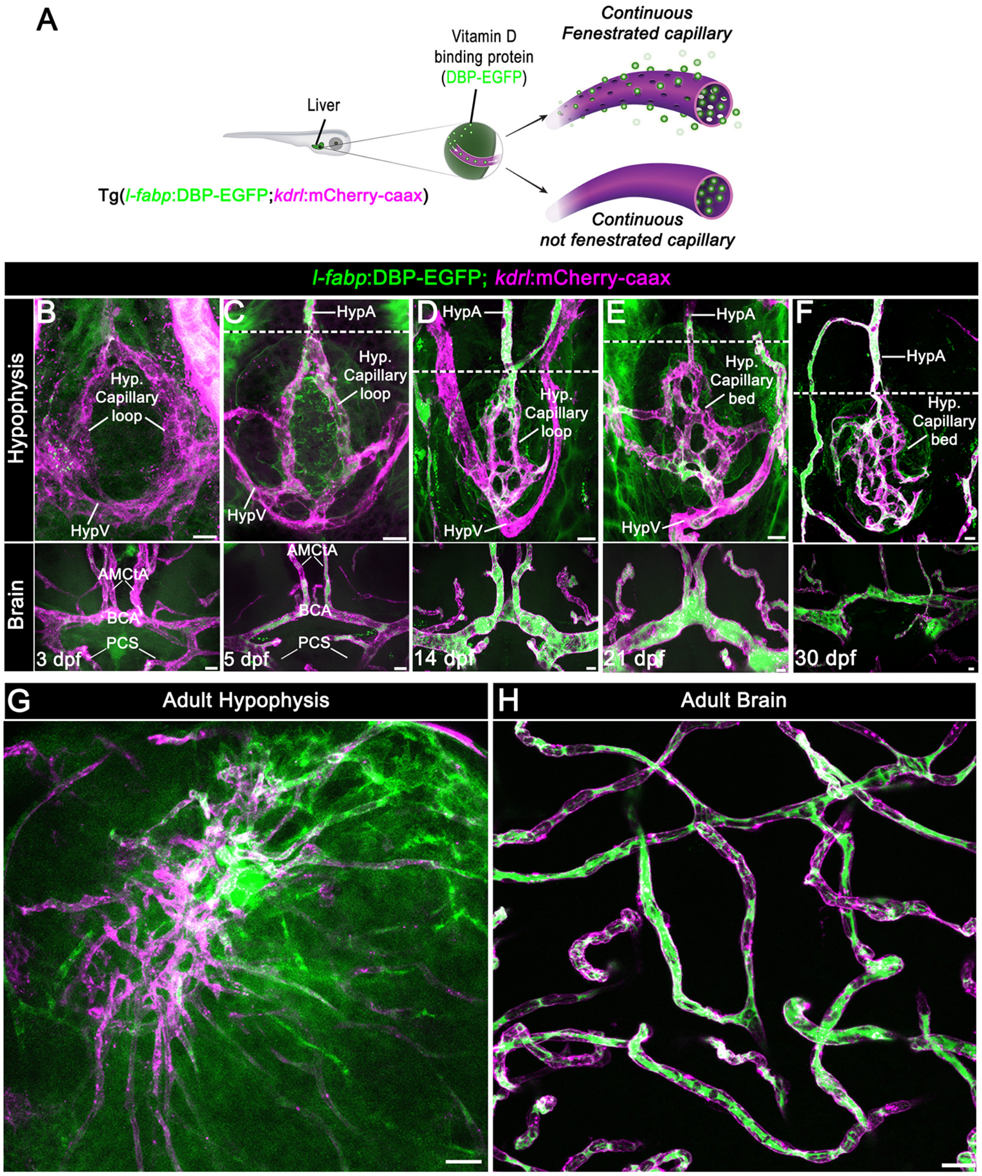

Fig. 1. Zebrafish neurohypophyseal vasculature is permeable to blood-borne proteins. (A) Scheme describing an endogenous biosensor for real-time monitoring of vascular permeability. Vitamin D-binding protein (DBP) fused to EGFP, expressed in hepatocytes under a liver-specific promoter (l-fabp) and secreted into the general circulation, served as permeability biosensor. (B-F) Wholemounts of double transgenic Tg(*l-fabp*:DBP-EGFP;*kdrl*:mCherry-caax) zebrafish at different developmental stages demonstrating extravasation of DBP-EGFP in the pituitary (top) but not in the brain (bottom). A functional permeability boundary is established between the capillary loop and hypophyseal artery (dotted lines). Scale bars: 5 µm. (G,H) Wholemounts of double transgenic Tg(*l-fabp*:DBP-EGFP;*kdrl*:mCherry-caax) adult zebrafish hypophysis (G) and brain (H) vasculature. Scale bars: 20 µm. AMCtA, anterior (rostral) mesencephalic central artery; BCA, basal communicating artery; HypA, hypophyseal artery; HypV, hypophyseal vein; PCS, posterior (caudal) communicating segment.

extends from the brain and connects to the capillary loop (dotted line in Fig. 1C). Thus, while the hypophyseal loop displayed extensive DBP-EGFP extravasation, the anterior part of the hypophyseal artery and the CNS vasculature retained the DBP-EGFP inside the vascular lumen. This permeability boundary between hypophyseal and brain vasculature became more prominent at juvenile stages (14-30 dpf), during which the hypophyseal capillary loop underwent extensive angiogenic sprouting. Specifically, the simple loop has transformed into an elaborated network of permeable microvessels (Fig. 1D-F) and, thereafter, formed highly complex hypophyseal capillary plexus in the adult fish (Fig. 1G). While the capillary plexus of the hypophysis maintained permeability to blood-borne protein, the brain vessels (Fig. 1H) remained non-permeable. As expected, hypophyseal capillaries of either 5 dpf larvae or adult zebrafish did not express the common BBB-associated tight junction marker claudin 5, whereas CNS vasculature displayed extensive anti-claudin 5 staining (Fig. 2). Thus, the functionalization of permeable hypophyseal capillaries correlated with the formation of BBB in CNS vasculature in the developing larvae.

Zebrafish hypophyseal capillaries contain fenestrae and caveolae

It has been reported that vertebrate hypophyseal capillaries contain multiple diaphragmed fenestral openings of about 60-80 nm in size (Farquhar, 1961; Gross et al., 1986; Holmes and Ball, 1974; Stan et al., 2012); however, there are no similar reports in zebrafish. To examine whether the blood vessels in the zebrafish hypophysis are fenestrated, we subjected zebrafish larvae and adults to transmission electron microscopy (TEM) (Fig. 3A,B) and scanning electron microscopy (cryo-SEM). Owing to the small size (~50×20 µm) of the hypophyseal capillary loop area in the larvae, we used the Tg(*oxtl*:EGFP) (Blechman et al., 2011) as a fluorescent landmark to identify the hypophysis for imaging (Fig. 3A). Our TEM imaging of hypophyseal sections demonstrated that diaphragmed fenestrae exist in the hypophyseal endothelia already in 5 dpf larvae (Fig. 3C). Moreover, both larval and adult hypophyseal capillaries contained diaphragmed fenestrae located along the endothelial wall, which appear as sieve-like structures (Fig. 3D). This was in contrast to the brain, where the BBB-containing endothelia contained tight junctions, dense basement membranes and lacked fenestrae

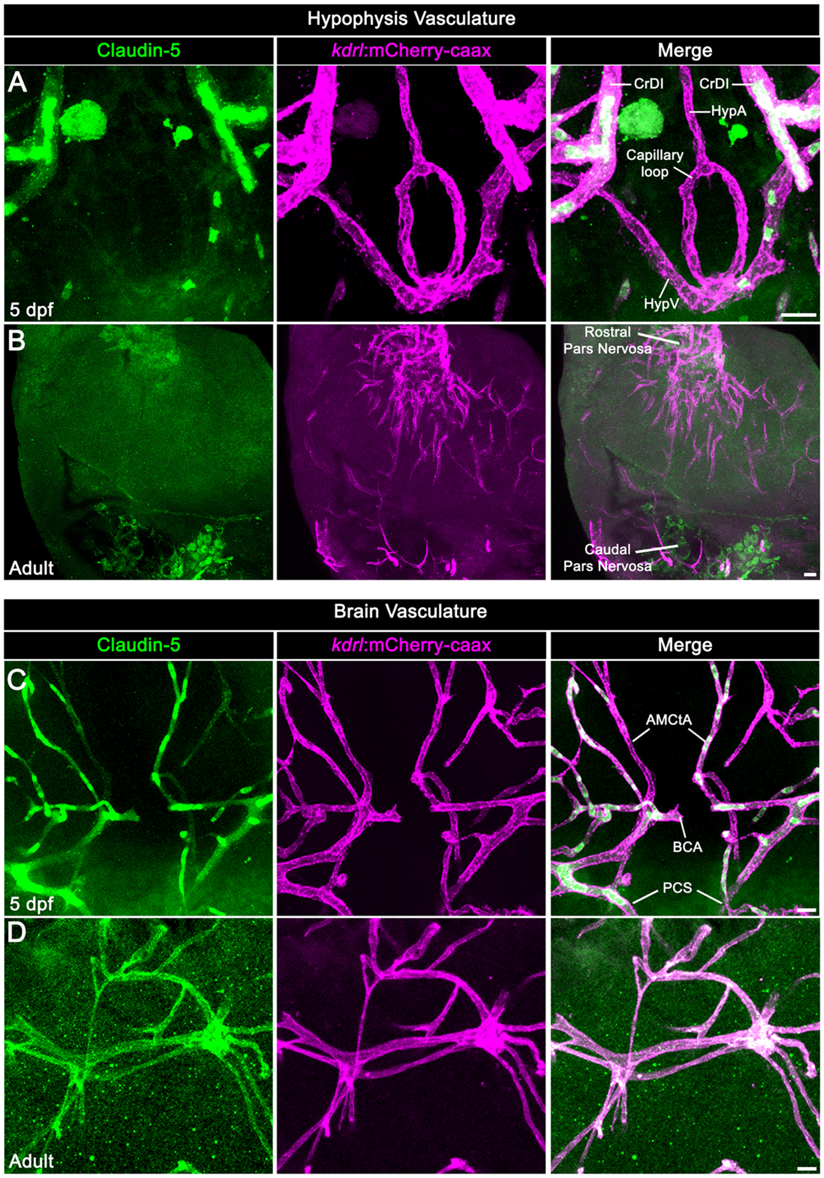

Fig. 2. Neurohypophyseal vasculature is devoid of the BBB marker protein claudin 5. (A,B) Claudin 5 expression in hypophyseal vessels of 5 dpf larvae (A) or adult (B) was detected by whole-mount immunofluorescence staining using anti-claudin 5 antibody. Tg(*kdrl*:mCherry-caax) zebrafish. (C,D) Claudin 5 expression in brain vasculature was detected by whole-mount immunofluorescence staining using anti-claudin 5 antibody in 5 dpf larvae (C) or adult (D) Tg(*kdrl*:mCherry-caax) zebrafish. AMCtA, anterior (rostral) mesencephalic central artery; BCA, basal communicating artery; CrDI, cranial division of the internal carotid artery; HypA, hypophyseal artery; HypV, hypophyseal vein; PCS, posterior (caudal) communicating segment. Scale bars: 5 µm in A,C; 20 µm in B,D.

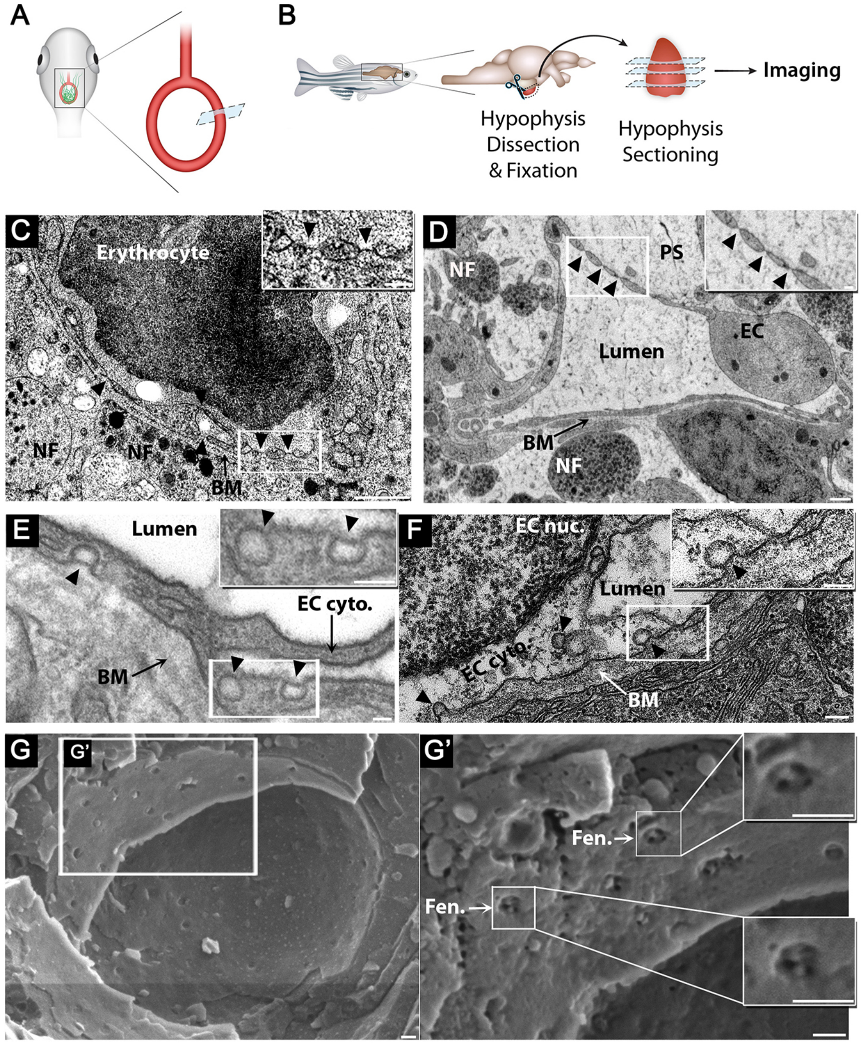

Fig. 3. Zebrafish hypophyseal endothelia contain diaphragmed fenestrae and caveolae. (A) Scheme describing TEM imaging of the hypophyseal capillary in zebrafish larvae. The hypophyseal *oxtl*:EGFP reporter was used as an anatomical landmark to localize the position of larval hypophysis prior to tissue preparation for TEM imaging. (B) Scheme describing TEM imaging of adult zebrafish hypophysis. Multiple ultrathin sections (60-80 nm) of the dissected hypophysis from adult zebrafish were submitted to TEM imaging. (C,D) TEM imaging of cross-section of larval (5 dpf) (C) and adult (D) showing hypophyseal fenestrated capillary contacting hypothalamic axonal nerve fibers (NF). Scale bars: 500 nm in C; 200 nm in D. Insets show higher magnification of diaphragmed fenestrae organized in a sieve-like manner. Fenestrae are indicated by arrowheads. Scale bars: 100 nm. (E,F) TEM imaging of hypophyseal endothelia containing abluminal, luminal and internalized caveolae indicated by arrowheads. Scale bars: 100 nm. Insets show higher magnification of internalized and surface caveolae with stomatal diaphragm. Scale bars: 100 nm. (G) Cryo-SEM imaging of fenestrated endothelia in adult zebrafish hypophysis. Higher magnifications (G′) of the hypophyseal fenestrated endothelial cell show the surface view of the fenestral diaphragm dissected into several openings by fibrils that converge at the center of the pore (insets). BM, basement membrane; EC, endothelial cell; EC cyto., endothelial cell cytoplasm; EC nuc., endothelial cell nucleus; Fen., fenestrae; NF, nerve fiber; PS, perivascular space. See related Fig. S1.

(Fig. S1). Finally, using cryo-SEM imaging, we obtained a surface view of the fenestral diaphragms, revealing that these diaphragms are dissected into several openings by fibrils that converge at the center of the pore (Fig. 3G). We conclude that zebrafish hypophyseal endothelium is fenestrated already at early developmental stages and remains fenestrated in adulthood.

In addition to fenestrae, zebrafish hypophysis contained classical neurovascular interfaces, including axonal swellings enriched with large dense core vesicles, which were detected near the endothelial basement membrane and perivascular space (Fig. 3C,D). Hypophyseal capillaries also contained caveolae. Open caveolar vesicles appeared on the luminal and abluminal sides of the capillary, whereas the 'internalized' cytoplasmic caveolar vesicles were localized inside the endothelial cell (Fig. 3E,F).

Zebrafish hypophyseal capillaries express two *Plvap* orthologs

We recently reported that 5 dpf zebrafish larvae express the *Plvap* ortholog *plvapb* (also known as *vsg1*) in the hypophyseal loop (Anbalagan et al., 2018). Our bioinformatic analysis revealed that the zebrafish genome contains two gene orthologs, *plvapa*, previously named *si:dkey-208k22.3*, and *plvapb* (Fig. 4A). The predicted zebrafish Plvapb protein resembles the secondary structure of the mammalian protein; however, it contains three coiled-coil domains compared with two in mammals. The predicted Plvapa protein, on the other hand, contains four coiled-coil domains and a longer C terminus (Fig. 4A and Fig. S2).

To explore the role of Plvap in hypophyseal endothelium, we examined the expression of *plvapa* and *plvapb* mRNAs by whole-mount fluorescence *in situ* hybridization at 3 and 5 dpf, which coincides with the developmental acquisition of hypophyseal vessel permeability, and in adult fish. The expression of *plvapb* mRNA already appeared in the hypophyseal vascular loop at 3 dpf, while *plvapa* expression was detected only at 5 dpf and persisted in the adult hypophyseal capillary plexus (Fig. 4C-E and Fig. S3). However, the expression of *plvapb* was considerably downregulated in the adult stage, suggesting that it functions in the developing hypophysis and not in the mature tissue (Fig. 4F and Fig. S3). In agreement with previous reports that PLVAP expression is downregulated in brain endothelia upon BBB formation (Hallmann et al., 1995; Umans et al., 2017; van der Wijk et al., 2019), expression of *plvapa* and *plvapb* was not detected in larval and adult brain vasculature (Fig. 4C,D, bottom; E,F, insets).

Mutation in *plvapb* leads to deficits in fenestral and stomatal diaphragms

To study the roles of zebrafish Plvap orthologs, we used the *plvapb*^{sa13080} mutant allele as well as transient CRISPR-mediated mutation (also known as a 'crispant') of *plvapa*. The *plvapb*^{sa13080} mutant allele contains a point mutation leading to a premature stop

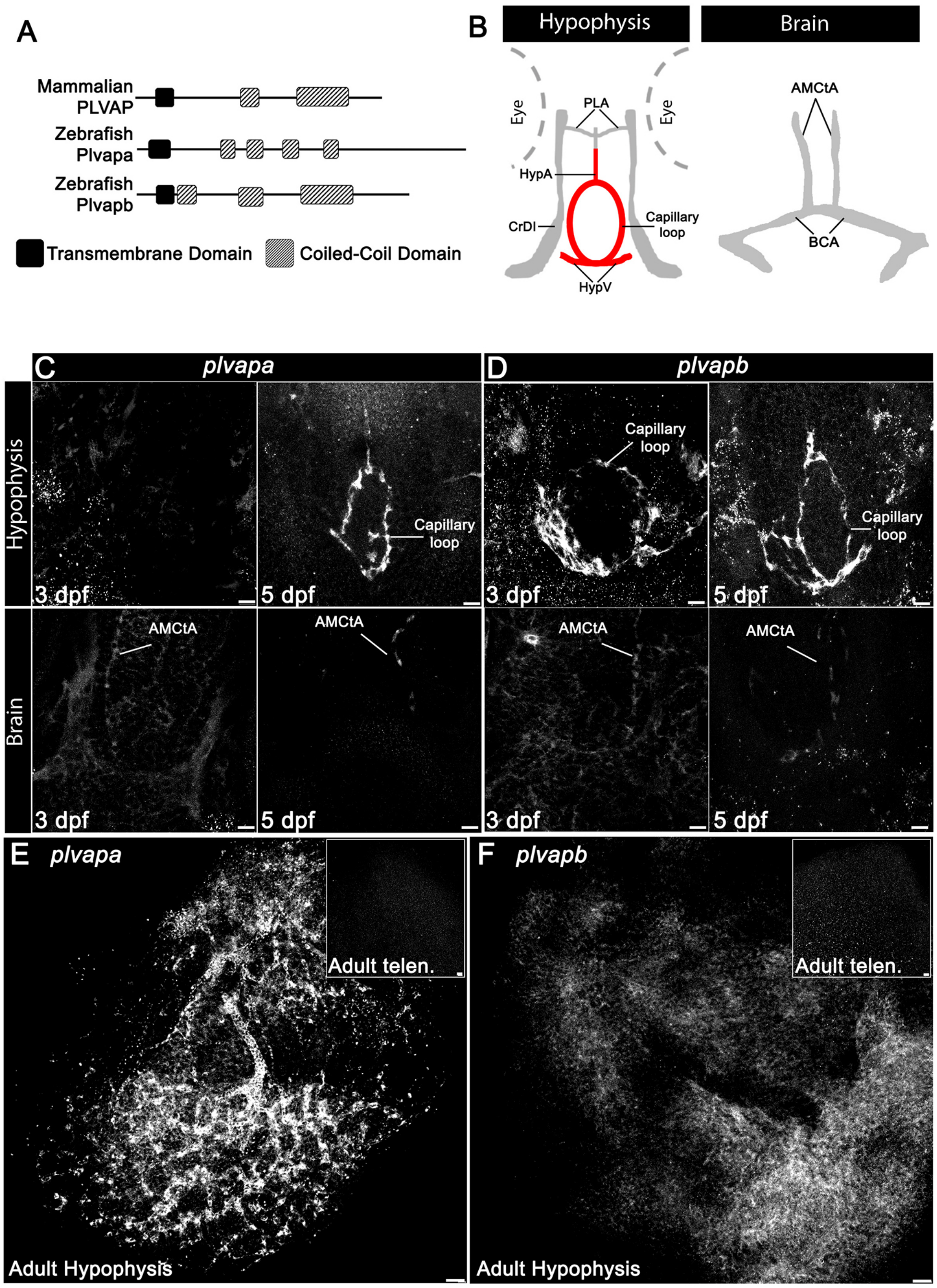

Fig. 4. Developmental expression of Plvap orthologs in the hypophyseal vasculature. (A) Schematic representation of the predicted secondary structure of zebrafish (Plvapa and Plvapb) and mammalian (PLVAP) proteins. (B) A scheme describing the major vasculature of the larval hypophysis and brain. (C,D) Whole-mount fluorescence *in situ* hybridization of zebrafish larvae at 3 or 5 dpf showing restricted *plvapa* (C) and *plvapb* (D) mRNA expression in the hypophyseal but not in the brain vasculature. Scale bars: 5 µm. (E,F) Whole-mount FISH of adult zebrafish showing restricted *plvapa* (E) and *plvapb* (F) mRNA expression in the hypophyseal but not in the brain vasculature. Scale bars: 20 µm. AMCtA, anterior (rostral) mesencephalic central artery; BCA, basal communicating artery; CrDI, cranial division of the internal carotid artery; HypA, hypophyseal artery; HypV, hypophyseal vein; PLA, palatocerebral artery. See related Figs S2 and S3.

codon, which is predicted to result in a truncated Plvapb protein lacking two out of three functionally important extracellular coiled-coil domains (Fig. S4A,B). The *plvapa* mutation was a large deletion in exon 1 that caused a truncation of trans-membranal protein domain (Fig. S4C,D). Injection of *plvapa* crispants into wild type or into a *plvapb* mutant resulted in a significant loss of hypophyseal endothelial cells and a poorly developed vasculature, precluding further analysis of fenestral formation and/or permeability (Fig. S5). Therefore, for the rest of this study, we proceeded to analyze the *plvapb*^{sa13080} mutant.

We first verified that the mutant *plvapb*^{sa13080} mRNA did not undergo altered splicing or non sense-mediated RNA decay, which are considered as major factors in eliciting gene compensation (El-Brolosy et al., 2019) (Fig. S4E,F). To further rule out possible genetic compensation, we compared the expression of *plvapa* and *plvapb* mRNAs in the vascular hypophyseal loop of *plvapb*$^{-/-}$ mutants versus wild type. We found no significant difference in *plvapb* and a slight decrease in *plvapa* levels (Fig. S6).

Quantitative TEM analysis of hypophyseal sections from adult *plvapb*$^{-/-}$ fish showed a significant loss of both fenestral (Fig. 5A-C and Fig. S7A) and stomatal (Fig. 5D-F and Fig. S7B) diaphragms. However, some diaphragms were still evident in the fenestral openings, probably owing to functional redundancy between *plvapa* and *plvapb* (Fig. 5B, black arrowheads). *plvapb*$^{-/-}$ fish displayed no differences in diaphragm thickness (Fig. 5G) of fenestrae and caveolae (Fig. 5H,I). Likewise, the mean diameter (Fig. 5G) of either fenestral or caveolar pores, with or without diaphragms, did not differ significantly between wild-type and mutant fish (Fig. 5J,K).

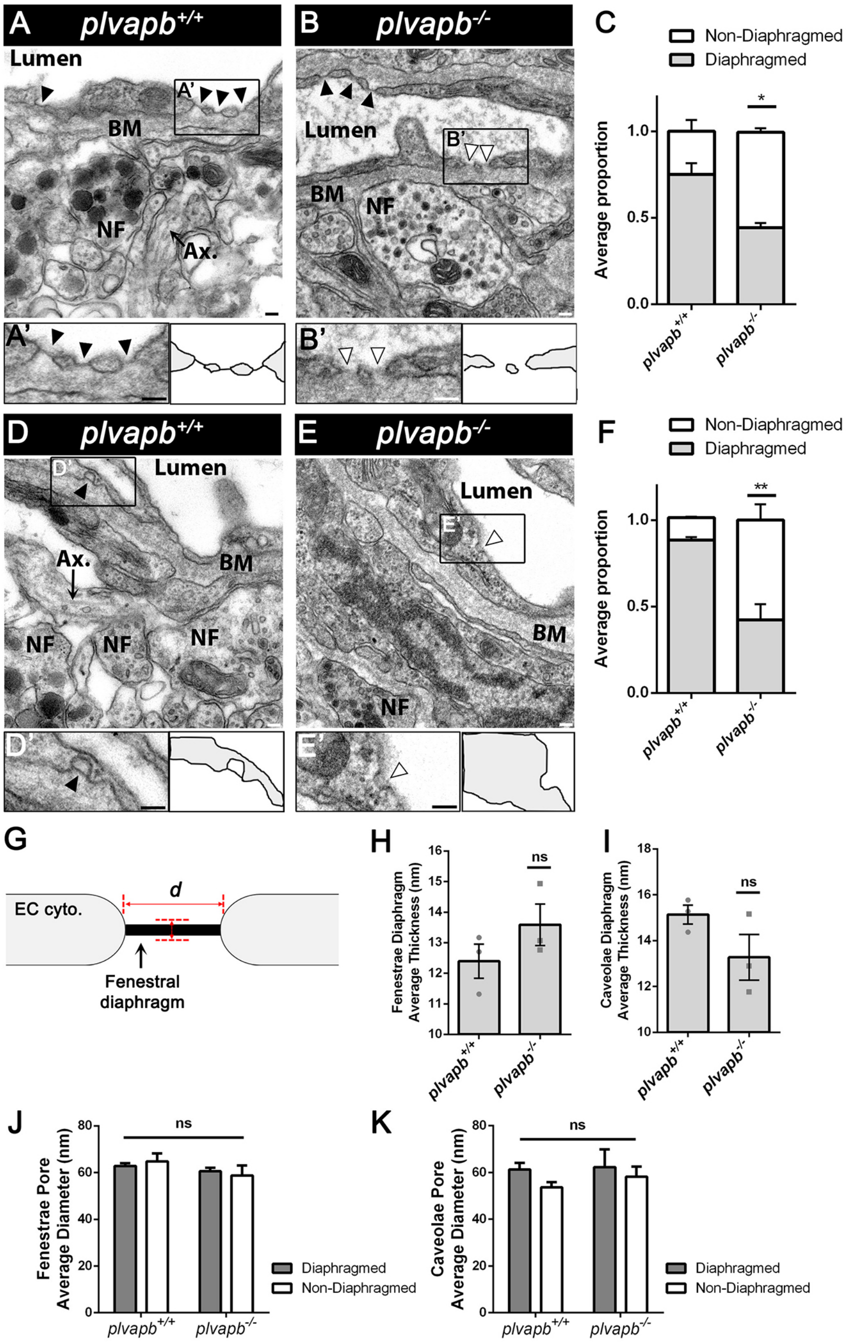

Fig. 5. Ultrastructural analysis of fenestral and stomatal diaphragms in wild-type versus *plvapb*$^{-/-}$ zebrafish hypophyseal endothelium. (A,B) TEM imaging of diaphragmed (black arrowheads) and non-diaphragmed (white arrowheads) fenestrae in the adult zebrafish hypophysis. (A′,B′). Higher magnification and graphical depiction of diaphragmed and non-diaphragmed fenestrae. (C) Graph showing the proportion of diaphragmed and non-diaphragmed fenestrae in the *plvapb*$^{+/+}$ versus *plvapb*$^{-/-}$ mutant fish. The proportion of diaphragmed $\left(\frac{n^{diaphragmed}}{n^{total}}\right)$ and non-diaphragmed $\left(\frac{n^{non-diaphragmed}}{n^{total}}\right)$ fenestrae was calculated in each blood capillary (5-25 capillaries per each biological repeat). The collated data of multiple capillaries measurements in each fish was averaged and plotted for each genotype. The proportion of complete diaphragms was significantly decreased in the mutant fish (*P<0.05; Welch two-sample t-test, n=3 for each genotype). (D,E) TEM imaging of diaphragmed (black arrowheads) and non-diaphragmed (white arrowheads) caveolae in the adult zebrafish hypophysis. (D′,E′) Higher magnification and graphical depiction of diaphragmed and non-diaphragmed caveolae. (F) Graph showing the proportion of diaphragmed and non-diaphragmed caveolae in the *plvapb*$^{+/+}$ versus *plvapb*$^{-/-}$ mutant fish. The proportion of diaphragmed and non-diaphragmed fenestrae was calculated as in C. The proportion of complete stomatal diaphragms was significantly decreased in the mutant fish (**P<0.01; Welch two-sample t-test, n=3 for each genotype). (G-K) Quantitative analyses the morphological parameters of fenestral and caveolar diaphragms in the wild type versus *plvapb*$^{-/-}$ mutant. The collated data of 5-25 blood capillaries in each biological repeat was averaged and plotted for each genotype. (G) Scheme describing how the diaphragm thickness and pore diameter of fenestrae and caveolae were measured. (H,I) Graphs showing mean fenestral (H) and caveolar (I) diaphragm thickness. No significant difference were found between *plvapb*$^{+/+}$ and *plvapb*$^{-/-}$ fish (ns, not significant; Welch two-sample t-test, n=3 for each genotype). (J,K) Graphs showing mean fenestral (J) and caveolar (K) pore diameter. No significant difference in the diameter of either diaphragmed or non-diaphragmed fenestral and caveolar openings was found between the *plvapb*$^{+/+}$ and *plvapb*$^{-/-}$ fish (ns=not significant; two-way ANOVA, n=3 for each genotype). Data are presented as mean±s.e.m.; individual data points are shown in H and I. Ax., axonal element; BM, basement membrane; NF, nerve fiber. Scale bars: 100 nm. See related Figs S4, S5, S6 and S7.

As mentioned, it has been suggested that Plvap is not required for fenestrae formation per se (Herrnberger et al., 2012; Stan et al., 2012). Therefore, focusing on hypophyseal vasculature, we examined whether developmental mutation in the *plvapb* ortholog affected fenestrae formation. Diaphragmed and non-diaphragmed fenestrae were counted along the length of the endothelial wall in each TEM image of adult zebrafish and their density was calculated. The mean density of fenestrae was more than 1.5 fenestrae per 10 µm of endothelium in *plvapb*$^{-/-}$ mutant fish, whereas in control *plvapb*$^{+/+}$ fish, the density was less then 0.5 fenestrae along the same endothelial length unit (Fig. 6A,B,E). However, the quantification of caveolar density, either diaphragmed or non-diaphragmed, along the endothelium revealed no significant difference between the genotypes (Fig. 6C-D,F). Notably, there were more abluminal than luminal caveolae in hypophyseal endothelia of both wild-type and mutant fish (Fig. S7C).

Taken together, these results suggest that developmental loss of function of *plvapb* impedes the formation of fenestral and caveolar diaphragms in hypophyseal endothelia. Moreover, the increased fenestrae density following *plvapb* loss of function may imply the existence of a Plvap-dependent regulatory feedback loop.

Plvap limits the rate of blood-borne protein transfer into the hypophysis

We hypothesized that loss of the fenestral diaphragm would affect the barrier function of neurohypophyseal endothelia. To directly decipher the role of *plvapb* in the passage of blood-borne proteins into the hypophysis parenchyma, we employed the Tg(*l-fabp*:DBP-

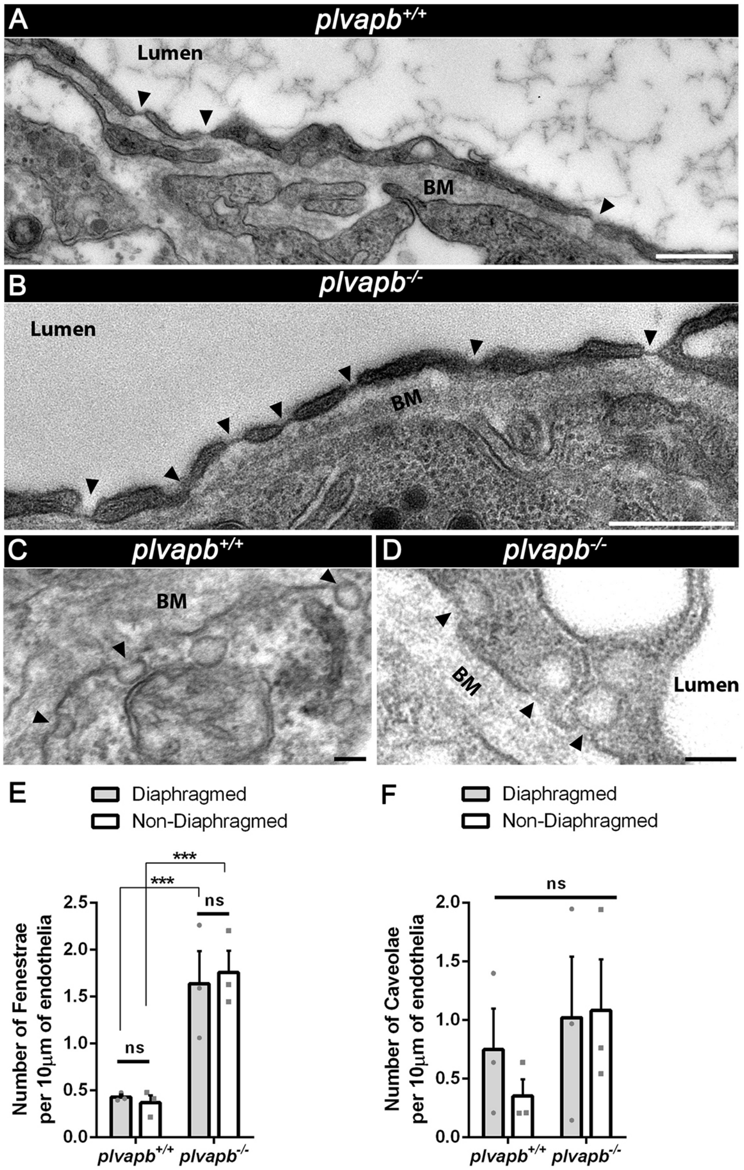

Fig. 6. Mutation in *plvapb* leads to increased density of fenestrae but not caveolae. (A,B) Representative TEM images of endothelial cells of the adult zebrafish hypophyses, showing the increased number of fenestrae (arrowheads) along the endothelium in the *plvapb*$^{-/-}$ mutant fish. Scale bars: 500 nm. (C,D) Representative TEM images of endothelial cells of adult zebrafish hypophyses showing multiple caveolae (arrowheads) along the endothelial wall. Scale bars: 100 nm. (E,F) Quantification of the linear density of diaphragmed and non-diaphragmed fenestrae (E) and caveolae (F) per length unit of endothelium. The number of these structures was counted and the endothelial cell length was measured within each blood capillary (5-25 blood capillaries per biological repeat). The density was calculated as the number of fenestrae and caveolae divided by endothelial wall length (nm). The density then was multiplied by 10^4 to represent the result as density per 10 μm of endothelial wall. A significant increase in the linear density of the diaphragmed and non-diaphragmed fenestrae, but not caveolae, was observed in the *plvapb*$^{-/-}$ mutants (***P<0.001, ns, not significant; two-way ANOVA, n=3 for each genotype). Data are mean±s.e.m. See related Fig. S7.

EGFP;*kdrl*:mCherry-caax) permeability reporter line (Fig. 1A). First, we examined the effect of loss of *plvapb* on hypophyseal vascular morphogenesis. Results showed no differences in the shape (roundness index) or total area of the hypophyseal capillary loop between *plvapb*$^{-/-}$ and control larvae (Fig. 7A-C). We next measured the accumulated fluorescence intensity of extravasated DBP-EGFP in the hypophyseal loop of fixed Tg(*l-fapb*:DBP-EGFP;*kdrl*:mCherry-caax) larvae, which were generated on the background of either *plvapb*$^{-/-}$ or its wild-type siblings (Fig. 7A). This analysis showed no significant differences between the wild-type and *plvapb*$^{-/-}$ mutant larvae (Fig. 7D), indicating that Plvapb does not affect the steady-state hypophyseal vascular permeability.

Next, we undertook real-time live-imaging approach to measure the kinetics of DBP-EGFP entry into the hypophyseal parenchyma by performing quantitative fluorescence recovery after photobleaching (FRAP) analysis in live embryos. Thus, live transgenic Tg(*l-fapb*: DBP-EGFP;kdrl:mCherry-caax) larvae were subjected to FRAP analysis using a two-photon microscope. Specifically, a distinct region of interest (ROI), external to hypophyseal blood capillary, was photobleached and DBP-EGFP extravasation was monitored in real time (Fig. 7E). The intensity of EGFP signal was measured before and after the bleaching and the normalized fluorescence intensity was plotted as a function of time (Fig. 7F). The half-time of fluorescent signal recovery ($T_{1/2}$), which was calculated using ImageJ FRAP Profiler tool (Fig. 7G), reflects the diffusion rate of the DBP-EGFP protein within the hypophysis parenchyma and, consequently, portrays the extravasation rate from the adjacent fenestrated blood capillary. Our FRAP analysis revealed that the recovery time of DBP-EGFP signal ($T_{1/2}$) in the *plvapb*$^{-/-}$ mutants was less than that of their wild-type siblings (4.685±0.705 s, n=8 versus 2.726±0.417 s, n=10, respectively), indicating a faster rate of DBP-EGFP extravasation in the absence of Plvapb (Fig. 7F,G). Taken together, our results provide the first direct proof that PLVAP, a structural protein of the fenestral and stomatal diaphragms, regulates the rate of blood-borne protein passage through the fenestrated endothelial wall into the hypophyseal parenchyma.

DISCUSSION

Fenestrated endothelia containing a PLVAP-positive diaphragm are found in various organs that communicate with the blood circulation

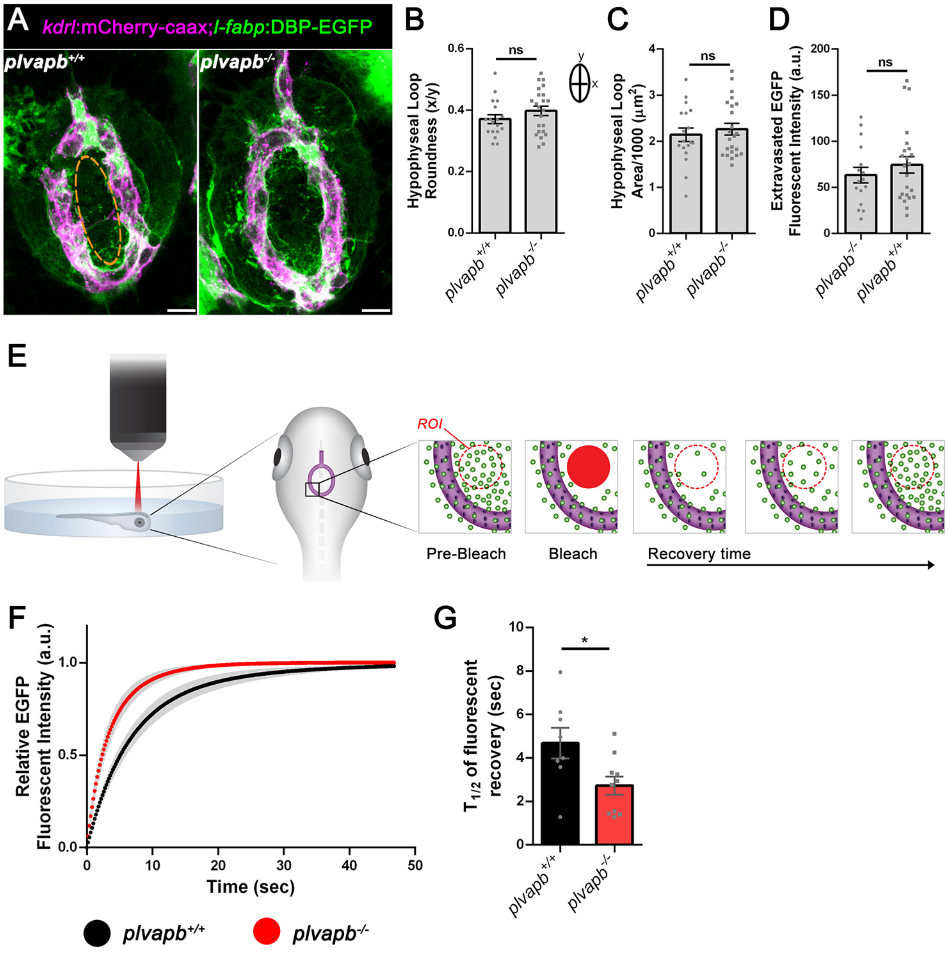

Fig. 7. Plvapb limits the transfer rate of blood-borne proteins into the hypophysis parenchyma. (A) Confocal maximal intensity images showing the hypophyseal capillary loop in *plvapb*$^{+/+}$ and *plvapb*$^{-/-}$ double transgenic Tg(*l-fabp*:DBP-EGFP;*kdrl*:mCherry-caax) zebrafish larvae (5 dpf). Scale bars: 10 µm. (B,C) Morphological analysis of hypophyseal capillary loop parameters, including roundness index [width (x)/length (y)] (B) and area (C). No significant differences were found between *plvapb*$^{+/+}$ (*n*=18) and *plvapb*$^{-/-}$ (*n*=23) fish (ns, not significant; Student's *t*-test). (D) Quantification of accumulated fluorescence intensity of the extravasated DBP-EGFP inside the hypophyseal capillary loop (dashed line in A, left panel) of fixed *plvapb*$^{+/+}$ (*n*=16) and *plvapb*$^{-/-}$ (*n*=23) larvae. No significant difference was found between the fish (ns, not significant; Student's *t*-test). (E) Schematic representation of the fluorescence recovery after photobleaching (FRAP) of extravasated DBP-EGFP in the hypophysis of live zebrafish larval. ROI, region of interest. (F) Real-time FRAP measurements of the intensity of extravasated DBP-EGFP signal in live *plvapb*$^{+/+}$ (*n*=8) and *plvapb*$^{-/-}$ (*n*=10) transgenic Tg(*l-fabp*:DBP-EGFP;*kdrl*:mCherry-caax) larvae (4 dpf). (G) $T_{1/2}$ of the fluorescence recovery after bleaching of DBP-EGFP. $T_{1/2}$ value (calculated using ImageJ FRAP Profiler tool) is significantly lower in the *plvapb*$^{-/-}$ mutant, indicating higher extravasation rate of blood-borne protein in mutant versus wild-type fish (*$P<0.05$; Student's *t*-test). a.u., arbitrary units. Data are mean±s.e.m.

by rapid exchange of solutes, hormones and blood-borne proteins. Classical examples of such tissues are endocrine glands, intestinal villi, kidney glomeruli and circumventricular organs (CVO) in the brain (Aird, 2007; Miyata, 2015, 2017; Stan, 2007). Here, we have investigated the role of PLVAP in regulating the passage of plasma proteins through the fenestrated endothelia of the hypophysis.

The deep brain location of the hypophysis and the fact that mammalian embryos develop *in utero* make it difficult to determine the developmental stage at which hypophyseal vascular permeability is established. Consequently, we lack information about the developmental acquisition of hypophyseal permeability. We therefore employed the genetically labeled permeability biosensor, DBP-EGFP, to visualize vascular permeability in the developing hypophysis of zebrafish. We found that a permeable hypophyseal capillary is established at a very early developmental stage and that this process is inversely correlated with the formation of BBB in CNS vasculature in the developing larvae. Notably, the hypophysis is regarded as one of several CVOs, which are permeable vascular interfaces devoid of BBB that surround the midline brain ventricles. These structures facilitate the molecular crosstalk between the brain and the peripheral circulation to regulate endocrine and metabolic function, thereby controlling homeostasis (Ganong, 2000; Miyata, 2017).

Previous studies have shown that the expression of Plvap becomes restricted to CVO vasculature upon formation of the BBB in other CNS blood vessels (Hallmann et al., 1995; Umans et al., 2017; van der Wijk et al., 2019). We show here that both *plvapa* and *plvapb*, the zebrafish orthologs of mammalian *Plvap*, are expressed by the embryonic hypophyseal endothelia and their confined pituitary expression coincides with the establishment of a sharp boundary between the permeable hypophyseal capillaries and the non-permeable brain vessels. What regulates the restricted *plvap* expression in the hypophysis and other CVOs is still unclear. We have recently shown that Vegf and TGFβ signaling are required to maintain vascular permeability as well as *plvapb* expression in the developing hypophysis (Anbalagan et al., 2018). Inhibition of both TGFβ and VEGF signaling pathways, but not of either of them alone, causes regression of choroid plexus vascular fenestrations (Maharaj et al., 2008). Moreover, VEGF plays a major role in induction of endothelial fenestrations and in maintaining their integrity in mature tissues (Hamilton et al., 2019; Kamba et al., 2006; Stan, 2007). However, it is currently unclear why comparable levels of VEGF and TGFβ induce fenestrae formation only in some vasculatures but not in others, which are often adjacent. Interestingly, we found a temporal separation between *plvapa* and *plvapb* expression: whereas *plvapb* is expressed by hypophyseal endothelia already at 3 dpf, during the angiogenic development of the primary capillary loop, the expression of *plvapa* is visible only later in development. This suggests that *plvapb* might be active during the initial acquisition of hypophyseal vascular permeability.

It has been reported that Plvap is crucial for formation of fenestral and stomatal diaphragms, yet it is not required for the formation of the fenestral pores themselves (Herrnberger et al., 2012; Ioannidou et al., 2006; Stan et al., 2012). We show here that *plvapb*$^{-/-}$ mutants exhibited significant loss of both fenestral and caveolar/stomatal diaphragms in the hypophysis. However, complete diaphragms were still found in some fenestrae and caveolae in these mutants. This phenotype might be because the *plvapb*^{sa13080} mutant is a hypomorph and therefore it displays a milder phenotype compared with mice and human. Alternatively, there might be functional redundancy between *plvapa* and *plvapb*, as both genes are expressed in the hypophyseal vasculature in both larvae and adult fish. In support of this assumption, we show here that the loss of *plvapa* alone or on the background of the *plvapb* mutants, lead to severe vascular morphology defects. This is in agreement with the previously observed severe defects in the vascular wall of subcutaneous capillaries in the Plvap knockout C57BL/6N mice, which suffered from edema and hemorrhages and premature death (Herrnberger et al., 2012).

Interestingly, we found that *plvapb*-deficient fish display increased density of fenestrae but not of caveolae in the hypophyseal endothelia. This phenotype was not found in the mouse *Plvap* knockout studies. Thus, the increased density of fenestrae in *plvapb*$^{-/-}$ mutant may imply the existence of a Plvap-dependent feedback mechanism, in which lower levels of Plvap protein activate an endothelial signaling cascade that drives fenestrae formation. Such a feedback mechanism may involve Vegf signaling, which is known to be crucial for fenestrae formation (Hamilton et al., 2019; Kamba et al., 2006; Stan, 2007).

Several studies on *Plvap* knockout mice have shown that the blood composition of these animals is severely disrupted, leading to hypoproteinemia, hypoalbuminemia and hypertriglyceridemia as a result of severe non-inflammatory protein-losing enteropathy (Herrnberger et al., 2012; Stan et al., 2012). These results were recently supported by independent case studies of human infants with homozygous nonsense mutation in *PLVAP*. The patients (<0.5 years old) suffered from severe protein-losing enteropathy caused by the absence of fenestral and stomatal diaphragms, and eventually died (Broekaert et al., 2018; Elkadri et al., 2015). These studies indicate that Plvap plays a crucial role in maintaining barrier function of fenestrated endothelium, preventing uncontrolled leakage of plasma proteins from the blood vessels (Guo et al., 2016). However, thus far there was no direct demonstration that Plvap restricts the passage of substances through the endothelial wall. By directly measuring the *in vivo* kinetics of plasma protein extravasation from the hypophyseal capillaries in *plvapb*$^{-/-}$ mutant versus wild-type larvae, we now show that Plvap limits the rate of passage of DBP-EGPF through the fenestrated endothelial wall. The deficiencies in both fenestral and caveolar diaphragms and the increased density of fenestrae in the hypophyseal endothelial cells that we observed may contribute to the faster rate of plasma protein extravasation into the interstitial space. To conclude, we provide here the first direct proof that Plvap, a structural protein of the fenestral diaphragm, regulates the entry of plasma proteins into the hypophysis.

MATERIALS AND METHODS

Animal models

Zebrafish were raised and bred according to standard protocols. Embryos were raised at 28.5°C in 30% Danieau's medium [0.17 mM NaCl, 0.21 mM KCl, 0.12 mM $MgSO_4$, 0.18 mM $Ca(NO_3)_2$, 0.15 mM HEPES (pH 7.4)] supplemented with 0.01 mg/l Methylene Blue. Prior to all labeling processes (detailed below), medium was supplemented with 8 mM PTU (1-phenyl-2-thiourea; Sigma-Aldrich) to avoid formation of melanin pigments. The PTU was added at the beginning of gastrulation at ∼5 h post fertilization (hpf) and no later than 24 hpf, and was kept in the medium until embryo fixation or live imaging.

DNA extraction and genotyping

DNA for genotyping was attained from clipped fins of adult fish or from fixed samples after staining. DNA was extracted by submersion of the tissue samples in 50 mM NaOH, incubation for 40 min at 95°C, cool down for 5 min at 4°C, followed by neutralization with 1 M Tris-HCl (pH 7.5; 1/10 of lysate volume). The lysate containing the genomic DNA was diluted 1:10 in double distilled H_2O and used for DNA amplification. The genomic region of interest was amplified by using taqDNA Polymerase Master Mix Red 2× reaction mix (Ampliqon). To genotype for the *plvapb*^{sa13080} allele, the amplified DNA region was detected by 0.8-1% agarose gel electrophoresis, then extracted and purified by using the NucleoSpin Gel and PCR Clean-up (Macherey-Nagel). Purified DNA fragments were sequenced by the Biological Services Unit at the Weizmann Institute of Science. Results were analyzed by ApE-A software (version 2.0, by M. Wayne Davis, University of Utah, USA). To genotype for the *plvapa* crispants the amplified DNA region in exon 1 was detected by 3% agarose. See Table S2 for oligonucleotide sequences.

Quantitative real-time PCR

For qRT-PCR, RNA in cell lysate was reverse-transcribed using Oligo-dT primer and SuperScript II reverse transcriptase (Invitrogen) according to the manufacturer's protocol. Transcript levels were determined by 7900HT Fast Real-Time PCR System (Applied Biosystems) using the Platinum SYBR Green qPCR SuperMix-UDG (Invitrogen). Actin β was used as reference gene and ΔΔCT analysis was performed as described elsewhere (Schmittgen and Livak, 2008).

Whole-mount fluorescence *in situ* hybridization and immunofluorescence staining

Whole-mount zebrafish larva RNA fluorescence *in situ* hybridization was performed as described previously (Wircer et al., 2017). For RNA probe synthesis, partial coding sequences of the *plvapa* and *plvapb* genes were amplified by PCR, using the T7 polymerase (Roche), and purified with a PCR clean-up kit. The purified products served as a template for synthesis of digoxigenin-labeled antisense mRNA probes using the DIG RNA labeling mix (Roche). The probes were then purified with RNAeasy mini kit (Qiagen) and diluted in prehybridization solution [50% formamide in double distilled H_2O, 5×SSC, 50 µg/ml heparin, 500 µg/ml yeast tRNA and 0.1% Tween-20 (pH ∼6.0)] to a working concentration of 200 ng/250 µl. See Table S2 for oligonucleotide sequences.

For immunofluorescence staining, larvae and freshly dissected adult hypophyses were first fixed overnight in 4% PFA and then washed in PBS (3×10 min). The samples were then permeabilized with PBSTx (Triton X100 0.5%; 3×20 min) and blocked in 500 µl of blocking solution (PBS+10% goat serum+1% DMSO+0.5% Triton X100) for 1 h at room temperature. The solution was then replaced with 200 µl of fresh blocking solution with anti-Cldn5 primary antibody at 1:50 concentration and incubated overnight at 4°C. Samples were washed with PBSTx (4×30 min) and treated with 200 µl of secondary antibodies in blocking solution at 1:200 concentration overnight at 4°C. Then, samples were washed with PBST (Tween 0.1%; 3×30 min) and transferred to graded concentrations of glycerol (25→50→75%). Prior to imaging, the jaws were removed and the larvae were mounted ventrally on the slide. See Table S1 for antibody details.

Sequence analysis of the zebrafish Plvap orthologs

The analysis of Plvapa and Plvapb proteins was performed by using Expasy Proteomics tools server (www.expasy.org/proteomics). Specifically, the programs InterPro (www.ebi.ac.uk/interpro/) (Mitchell et al., 2018) and Phobius (phobius.sbc.su.se/) (Käll et al., 2004) were used for detection of transmembrane domains and COILS (embnet.vital-it.ch/software/COILS_form.html) for coiled-coil domains.

Generation of *plvapa* crispants

For generation of *plvapa* crispant mutants, simultaneous injection of two gRNAs targeting *plvapa* were injected into one-cell stage embryos from an in-cross of heterozygous *plvapb*$^{+/-}$ fish on the background of Tg(*fli1*:nucEGFP). Larvae then were genotyped for crispants bearing the expected *plvapa* deletion ('cut') or crispant in which no deletion was detected ('uncut'). For mock crispant control, we employed the non-relevant two gRNAs targeted to mCherry. All target gRNAs were designed by CHOPCHOP web tool (chopchop.cbu.uib.no/). See Table S1 oligonucleotide sequences.

Image acquisition

For transmission electron microscopy (TEM) imaging of hypophyseal fenestrated endothelia, whole hypophyses from adult zebrafish were dissected and immediately frozen in HPM010 high-pressure freezing machine (Bal-Tec). Samples were subsequently freeze substituted in an AFS2 freeze-substitution device (Leica Microsystems) in anhydrous acetone containing 2% glutaraldehyde and 0.2% tannic acid for 3 days at −90°C and then warmed up to −30°C over 24 h. Samples were washed in anhydrous acetone, incubated for 1 h at room temperature with 2% osmium tetroxide and 2% uranyl acetate dissolved in ethanol. The samples were then washed with anhydrous acetone and infiltrated for 5-7 days at room temperature in increasing concentration of Epon in acetone.

For TEM imaging of hypophyseal and brain endothelia during early development, the transgenic Tg(*oxtl*:EGFP) zebrafish larvae (5 dpf) were first anesthetized with tricaine and a small incision was made on the dorsal part of the scalp, followed by immediate fixation with fixative buffer (4% PFA, 0.2% glutaraldehyde, 0.1 M cacodylate and 5 mM $CaCl_2$) overnight. The larvae were then embedded in 3.4% Noble Agar (DIFCO) and sectioned using a vibratome (OTS-4000, Electron Microscopy Sciences). EGFP-positive slices (∼200 µm thick), which embrace the hypophysis, were identified by fluorescence microscopy and were selected for further processing using TEM.

For quantitative ultrastructural analyses of fenestrae and caveolae TEM imaging of sectioned hypophyses from adult fish was performed. The whole hypophysis was dissected and immediately fixed in fixative buffer (4% PFA, 2% glutaraldehyde, 0.1 M cacodylate and 5 mM $CaCl_2$) overnight. The adult whole hypophyses and larval EGFP-positive samples were then washed in 0.1 M cacodylate buffer and incubated in 1% osmium tetraoxide, 0.5% potassium dichromate, 0.5% potassium hexacyanoferrate in 0.1 M cacodylate for 1 h. Samples were rinsed in 0.1 M cacodylate and then in double distilled H_2O. Next, the samples were incubated in 2% uranyl acetate for 1 h covered with aluminium foil. Afterwards, samples were dehydrated in ethanol series and infiltrated for 5-7 days at room temperature in increasing concentration of Epon with ethanol.

The Epon-infiltrated samples were polymerized in at 60°C for 48 h. Ultrathin sections (60-80 nm) were mounted on 200 mesh grids (Electron Microscopy Sciences) supported with carbon-coated nitrocellulose film. The ultrathin sections double stained with 2% uranyl acetate in double distilled H_2O and Reynolds lead citrate (Reynolds, 1963) and imaged using a Tecnai T12 electron microscope operating at 120 kV with an ES500W Erlangshen CCD camera (Gatan) or an Eagle 2 K X 2 K CCD camera (FEI).

For visualizing the fenestrae and caveolae, image montages of large areas that included either longitudinal or cross-sections of endothelial cells were acquired with the Eagle CCD camera using the SerialEM program for TEM automated acquisition (Mastronarde, 2005). Alignment of montaged images was conducted using the ‘justblend’ script included in the IMOD software package (Kremer et al., 1996).

For cryo-scanning electron microscopy (SEM), adult zebrafish hypophyses were dissected and fixed in 4% PFA and were then submitted to Cryo-SEM imaging as described previously (Gur et al., 2018). In short, dissected pituitaries were cryo-immobilized in a high-pressure freezing device (HPM10; Bal-Tec). The frozen samples were transferred to a freeze-fracture device (BAF60; Bal-Tec), where they were freeze fractured and then coated with a 4 nm layer of Pt/C. Samples were then observed by high-resolution SEM (Ultra 55, Zeiss) using secondary electrons and an in-lens detector, maintaining the frozen hydrated state by using a cryo-stage operating at a working temperature of −120°C. Image processing was performed using ImageJ software.

Fluorescence recovery after photobleaching

Fluorescence recovery after photobleaching (FRAP) was performed in live Tg(*l-fabp*:DBP-EGFP;kdrl:mCherry-caax) 4-day-old wild-type and *plvapb*$^{-/-}$ mutant larvae, using the LSM7 MP laser scanning microscope (Zeiss) with modified Achroplan X 40 0.8W, NA 1.0. The larvae were anesthetized with tricaine in Danieau’s solution without Methylene Blue. Larvae were then mounted in ∼30 µl of low melting point agarose (1%) in a petri dish (60×15 mm) and covered with Danieau’s solution. For bleaching, the laser was set on 940 nm, 100% power for 20 iterations directed on multiple sequential small (∼3 µm) regions of interest (ROIs) outside the hypophyseal capillary. For background signal, a region outside the pituitary was also bleached. For reference signal, an additional region inside the pituitary capillary loop was measured, but not bleached. Consecutive time series images were taken before (*n*=10) and immediately after the photobleaching (290). Acquisition specifications were: Image dimension, 164×164 pixels (scaled: 37.96 µm×37.96 µm); objective, W Plan-Apochromat 20×/1.0 DOC VIS-IR M27 75 mm; scan zoom, X-11.2, Y-11.2; pixel time, 1.23 µs; frame time, 38.96 ms. The raw datasets were first prefiltered with a Gaussian blur 3D (x=0, y=0, z=5), thereby averaging every five images (the first and last five images were excluded).

The EGFP fluorescent signal data were then normalized to the background signal and the average fluorescence intensity after photobleaching over time was plotted. Each time point was normalized to the highest intensity value so that the maximal fluorescence recovery value in both genotypes is now comparable. Average recovery half-time ($T_{1/2}$) of the extravasated DBP-EGFP signal was calculated for wild-type and mutant groups. All the calculations were performed using the ImageJ FRAP Profiler tool (worms.zoology.wisc.edu/research/4d/4d.html).

Quantification and statistical analysis

Confocal images were analyzed using the open source ImageJ software. To quantify hypophyseal capillary loop morphology and permeability in fixed larvae, the *z*-stacks encompassing the hypophyseal loop were summed up using the ImageJ Z-project tool. To assess vascular permeability, the mean fluorescence intensity inside the loop area was measured (see Fig. 7A, dotted line). A region of interest of constant size in the non-permeable region in the brain parenchyma was also measured for background correction. Specifically, the values of the background fluorescence were subtracted from the values of the inside loop area and averaged for each genotype group. Likewise, to quantify fluorescence *in situ* hybridization signals, the integrated fluorescence intensity was measured within the hypophyseal capillary loop. A region of interest of constant size in the non-permeable region in the brain parenchyma was measured for background correction.

For the quantitative analyses of fenestrae and caveolae ultrastructure by TEM, the hypophyses from wild-type *plvapb*$^{+/+}$ or *plvapb*$^{-/-}$ mutant fish were dissected and submitted to sample preparation and TEM imaging, as described above. The fenestrae and caveolae vesicles were identified by their unique fine structure and the pore diameter (50-80 nm for fenestrae; 50-100 nm for caveolae) according to previous ultrastructural studies on endothelial cells (Aird, 2007; Elfvin, 1965; Palade and Bruns, 1968; Rhodin, 1962; Stan, 2005, 2007).

For quantification, multiple ultrathin sections of *plvapb*$^{+/+}$ (*n*=3) and *plvapb*$^{-/-}$(*n*=3) covering between 5 and 25 blood capillaries were imaged and quantified by using ImageJ software in each of the sampled biological repeats of the different genotypes. The collated data of multiple capillary measurements in each fish were averaged and plotted for each genotype. For ultrastructural analysis of fenestral and stomatal diaphragms, the proportion of diaphragmed versus non-diaphragmed structures was calculated in each blood capillary. This was performed by dividing the number of diaphragmed and non-diaphragmed fenestrae/surfaced caveolae by the total number of these structures.

For quantification of average fenestral and stomatal diaphragm thickness, the thickness of each diaphragm was measured three times using a line drawing tool in ImageJ and averaged. For quantification of average fenestral and caveolar pore diameter, the diameter of each pore was measured three times using a line drawing tool in ImageJ and averaged. The collated data of 5-25 blood capillaries in each fish was averaged and plotted for each genotype.

For quantification of the linear density of diaphragmed and non-diaphragmed fenestrae and caveolae per length unit of endothelium, the number of these structures was counted and the endothelial cell length was measured within each blood capillary. The density was calculated as the number of fenestrae and caveolae divided by endothelial wall length (nm). The density then was multiplied by 10^4 to present the result as density per 10 µm of endothelial wall.

All data were tested for normality using the Shapiro-Wilk test. Student's *t*-test or Welch two-sample *t*-test was used for comparisons between two groups. Two-way ANOVA was used for comparison of pore diameters and linear density of the diaphragmed and non-diaphragmed fenestrae and caveolae between the $\mathit{plvapb}^{+/+}$ and $\mathit{plvapb}^{-/-}$ fish, as well as for comparison of abluminal and luminal caveola density in $\mathit{plvapb}^{+/+}$ versus $\mathit{plvapb}^{-/-}$ fish. Statistical significance was determined as $P<0.05$. Data are presented as mean±standard error of the mean (s.e.m.).

Acknowledgements

We thank Roy Hofi for animal care, Vyacheslav Kalchenko for helping with the FRAP experiments, Ron Rotkopf for statistical analysis, Nitzan Konstantin for English editing, and Tal Bigdary and Noa David for graphical schemes. The $\mathit{plvapb}^{sa13080}$ mutant was generated and provided by the Sanger Institute Zebrafish Mutation Project.

Competing interests

The authors declare no competing or financial interests.

Author contributions

Conceptualization: L.G., G.L.; Methodology: L.G., J.B., E.S., D.G.; Formal analysis: L.G.; Resources: J.B., B.A.-A., G.L.; Data curation: L.G.; Writing - original draft: L.G., G.L.; Writing - review & editing: L.G., E.S., D.G., B.A.-A., G.L.; Visualization: L.G., J.B., E.S., D.G.; Supervision: G.L.; Project administration: G.L.; Funding acquisition: G.L.

Funding

B.A.-A. is supported by the National Institutes of Health (EY026181, EY027083, P30EY025585) and by a Research to Prevent Blindness Challenge Grant. G.L. is supported by the Israel Science Foundation (1511/16), the United States-Israel Binational Science Foundation (2017325), the Minerva Foundation, the Adelis Metabolic Research Fund and the Yeda-Sela Center for Basic Research (in the frame of the Weizmann Institute). G.L. is an incumbent of the Elias Sourasky Professorial Chair. Deposited in PMC for release after 12 months.

Supplementary information

Supplementary information available online at
http://dev.biologists.org/lookup/doi/10.1242/dev.177790.supplemental

References

Aird, W. C. (2007). Phenotypic heterogeneity of the endothelium: I. Structure, function, and mechanisms. *Circ. Res.* **100**, 158-173. doi:10.1161/01.RES.0000255691.76142.4a

Anbalagan, S., Gordon, L., Blechman, J., Matsuoka, R. L., Rajamannar, P., Wircer, E., Biran, J., Reuveny, A., Leshkowitz, D., Stainier, D. Y. R. et al. (2018). Pituicyte cues regulate the development of permeable neuro-vascular interfaces. *Dev. Cell* **47**, 711-726.e715. doi:10.1016/j.devcel.2018.10.017

Blechman, J., Amir-Zilberstein, L., Gutnick, A., Ben-Dor, S. and Levkowitz, G. (2011). The metabolic regulator PGC-1{alpha} directly controls the expression of the hypothalamic neuropeptide oxytocin. *J. Neurosci.* **31**, 14835-14840. doi:10.1523/JNEUROSCI.1798-11.2011

Broekaert, I. J., Becker, K., Gottschalk, I., Körber, F., Dötsch, J., Thiele, H., Altmüller, J., Nürnberg, P., Hünseler, C. and Cirak, S. (2018). Mutations in plasmalemma vesicle-associated protein cause severe syndromic protein-losing enteropathy. *J. Med. Genet.* **55**, 637-640. doi:10.1136/jmedgenet-2018-105262

Ciofi, P., Garret, M., Lapirot, O., Lafon, P., Loyens, A., Prévot, V. and Levine, J. E. (2009). Brain-endocrine interactions: a microvascular route in the mediobasal hypothalamus. *Endocrinology* **150**, 5509-5519. doi:10.1210/en.2009-0584

El-Brolosy, M. A., Kontarakis, Z., Rossi, A., Kuenne, C., Günther, S., Fukuda, N., Kikhi, K., Boezio, G. L. M., Takacs, C. M., Lai, S.-L. et al. (2019). Genetic compensation triggered by mutant mRNA degradation. *Nature* **568**, 193-197. doi:10.1038/s41586-019-1064-z

Elfvin, L.-G. (1965). The ultrastructure of the capillary fenestrae in the adrenal medulla of the rat. *J. Ultrastruct. Res.* **12**, 687-704. doi:10.1016/S0022-5320(65)80056-9

Elkadri, A., Thoeni, C., Deharvengt, S. J., Murchie, R., Guo, C., Stavropoulos, J. D., Marshall, C. R., Wales, P., Bandsma, R., Cutz, E. et al. (2015). Mutations in Plasmalemma vesicle associated protein result in sieving protein-losing enteropathy characterized by hypoproteinemia, hypoalbuminemia, and hypertriglyceridemia. *Cell Mol. Gastroenterol. Hepatol.* **1**, 381-394.e387. doi:10.1016/j.jcmgh.2015.05.001

Farquhar, M. G. (1961). Fine structure and function in capillaries of the anterior pituitary gland. *Angiology* **12**, 270-292. doi:10.1177/000331976101200704

Filippini, A., Sica, G. and D'Alessio, A. (2018). The caveolar membrane system in endothelium: from cell signaling to vascular pathology. *J. Cell. Biochem.* **119**, 5060-5071. doi:10.1002/jcb.26793

Ganong, W. F. (2000). Circumventricular organs: definition and role in the regulation of endocrine and autonomic function. *Clin. Exp. Pharmacol. Physiol.* **27**, 422-427. doi:10.1046/j.1440-1681.2000.03259.x

Gross, P. M., Sposito, N. M., Pettersen, S. E. and Fenstermacher, J. D. (1986). Differences in function and structure of the capillary endothelium in the supraoptic nucleus and pituitary neural lobe of rats. Evidence for the supraoptic nucleus as an osmometer. *Neuroendocrinology* **44**, 401-407. doi:10.1159/000124678

Guo, L., Zhang, H., Hou, Y., Wei, T. and Liu, J. (2016). Plasmalemma vesicle-associated protein: a crucial component of vascular homeostasis. *Exp. Ther. Med.* **12**, 1639-1644. doi:10.3892/etm.2016.3557

Gur, D., Nicolas, J. D., Brumfeld, V., Bar-Elli, O., Oron, D. and Levkowitz, G. (2018). The dual functional reflecting iris of the Zebrafish. *Advanced Science* **5**, 1800338. doi:10.1002/advs.201800338

Gutnick, A., Blechman, J., Kaslin, J., Herwig, L., Belting, H.-G., Affolter, M., Bonkowsky, J. L. and Levkowitz, G. (2011). The hypothalamic neuropeptide oxytocin is required for formation of the neurovascular interface of the pituitary. *Dev. Cell* **21**, 642-654. doi:10.1016/j.devcel.2011.09.004

Hallmann, R., Mayer, D. N., Berg, E. L., Broermann, R. and Butcher, E. C. (1995). Novel mouse endothelial cell surface marker is suppressed during differentiation of the blood brain barrier. *Dev. Dyn.* **202**, 325-332. doi:10.1002/aja.1002020402

Hamilton, B. J., Tse, D. and Stan, R. V. (2019). Phorbol esters induce PLVAP expression via VEGF and additional secreted molecules in MEK1-dependent and p38, JNK and PI3K/Akt-independent manner. *J. Cell. Mol. Med.* **23**, 920-933. doi:10.1111/jcmm.13993

Herrnberger, L., Seitz, R., Kuespert, S., Bös, M. R., Fuchshofer, R. and Tamm, E. R. (2012). Lack of endothelial diaphragms in fenestrae and caveolae of mutant Plvap-deficient mice. *Histochem. Cell Biol.* **138**, 709-724. doi:10.1007/s00418-012-0987-3

Holmes, R. L. and Ball, J. N. (1974). *The Pituitary Gland: A Comparative Account*: University Press.

Ioannidou, S., Deinhardt, K., Miotla, J., Bradley, J., Cheung, E., Samuelsson, S., Ng, Y.-S. and Shima, D. T. (2006). An in vitro assay reveals a role for the diaphragm protein PV-1 in endothelial fenestra morphogenesis. *Proc. Natl. Acad. Sci. USA* **103**, 16770-16775. doi:10.1073/pnas.0603501103

Käll, L., Krogh, A. and Sonnhammer, E. L. L. (2004). A combined transmembrane topology and signal peptide prediction method. *J. Mol. Biol.* **338**, 1027-1036. doi:10.1016/j.jmb.2004.03.016

Kamba, T., Tam, B. Y. Y., Hashizume, H., Haskell, A., Sennino, B., Mancuso, M. R., Norberg, S. M., O'Brien, S. M., Davis, R. B., Gowen, L. C. et al. (2006). VEGF-dependent plasticity of fenestrated capillaries in the normal adult microvasculature. *Am. J. Physiol. Heart Circ. Physiol.* **290**, H560-H576. doi:10.1152/ajpheart.00133.2005

Kremer, J. R., Mastronarde, D. N. and McIntosh, J. R. (1996). Computer visualization of three-dimensional image data using IMOD. *J. Struct. Biol.* **116**, 71-76. doi:10.1006/jsbi.1996.0013

Liu, F., Pogoda, H. M., Pearson, C. A., Ohyama, K., Lohr, H., Hammerschmidt, M. and Placzek, M. (2013). Direct and indirect roles of Fgf3 and Fgf10 in innervation and vascularisation of the vertebrate hypothalamic neurohypophysis. *Development* **140**, 1111-1122. doi:10.1242/dev.080226

Maharaj, A. S. R., Walshe, T. E., Saint-Geniez, M., Venkatesha, S., Maldonado, A. E., Himes, N. C., Matharu, K. S., Karumanchi, S. A. and D'Amore, P. A. (2008). VEGF and TGF-β are required for the maintenance of the choroid plexus and ependyma. *J. Exp. Med.* **205**, 491-501. doi:10.1084/jem.20072041

Mastronarde, D. N. (2005). Automated electron microscope tomography using robust prediction of specimen movements. *J. Struct. Biol.* **152**, 36-51. doi:10.1016/j.jsb.2005.07.007

Milici, A. J., Peters, K.-R. and Palade, G. E. (1986). The endothelial pocket: a new structure in fenestrated endothelia. *Cell Tissue Res.* **244**, 493-499. doi:10.1007/BF00212526

Mitchell, A. L., Sangrador-Vegas, A., Luciani, A., Madeira, F., Nuka, G., Salazar, G. A., Chang, H.-Y., Richardson, L. J., Qureshi, M. A., Fraser, M. I. et al. (2018). InterPro in 2019: improving coverage, classification and access to protein sequence annotations. *Nucleic Acids Res.* **47**, D351-D360. doi:10.1093/nar/gky1100

Miyata, S. (2015). New aspects in fenestrated capillary and tissue dynamics in the sensory circumventricular organs of adult brains. *Front. Neurosci.* **9**, 390. doi:10.3389/fnins.2015.00390

Miyata, S. (2017). Advances in understanding of structural reorganization in the hypothalamic neurosecretory system. *Front. Endocrinol.* **8**, 275. doi:10.3389/fendo.2017.00275

Palade, G. E. and Bruns, R. R. (1968). Structural modulations of plasmalemmal vesicles. *J. Cell Biol.* **37**, 633-649. doi:10.1083/jcb.37.3.633

Reynolds, E. S. (1963). The use of lead citrate at high pH as an electron-opaque stain in electron microscopy. *J. Cell Biol.* **17**, 208-212. doi:10.1083/jcb.17.1.208

Rhodin, J. A. (1962). The diaphragm of capillary endothelial fenestrations. *J. Ultrastruct. Res.* **6**, 171-185. doi:10.1016/S0022-5320(62)90052-7

Schaeffer, M., Hodson, D. J. and Mollard, P. (2014). The blood-brain barrier as a regulator of the gut-brain axis. *Front. Horm. Res.* **42**, 29-49. doi:10.1159/000358313

Schmittgen, T. D. and Livak, K. J. (2008). Analyzing real-time PCR data by the comparative CT method. *Nat. Protoc.* **3**, 1101-1108. doi:10.1038/nprot.2008.73

Stan, R. V. (2005). Structure of caveolae. *Biochim. Biophys. Acta* **1746**, 334-348. doi:10.1016/j.bbamcr.2005.08.008

Stan, R. V. (2007). Endothelial stomatal and fenestral diaphragms in normal vessels and angiogenesis. *J. Cell. Mol. Med.* **11**, 621-643. doi:10.1111/j.1582-4934.2007.00075.x

Stan, R. V., Kubitza, M. and Palade, G. E. (1999). PV-1 is a component of the fenestral and stomatal diaphragms in fenestrated endothelia. *Proc. Natl. Acad. Sci. USA* **96**, 13203-13207. doi:10.1073/pnas.96.23.13203

Stan, R. V., Tkachenko, E. and Niesman, I. R. (2004). PV1 is a key structural component for the formation of the stomatal and fenestral diaphragms. *Mol. Biol. Cell* **15**, 3615-3630. doi:10.1091/mbc.e03-08-0593

Stan, R. V., Tse, D., Deharvengt, S. J., Smits, N. C., Xu, Y., Luciano, M. R., McGarry, C. L., Buitendijk, M., Nemani, K. V., Elgueta, R. et al. (2012). The diaphragms of fenestrated endothelia: gatekeepers of vascular permeability and blood composition. *Dev. Cell* **23**, 1203-1218. doi:10.1016/j.devcel.2012.11.003

Umans, R. A., Henson, H. E., Mu, F., Parupalli, C., Ju, B., Peters, J. L., Lanham, K. A., Plavicki, J. S. and Taylor, M. R. (2017). CNS angiogenesis and barriergenesis occur simultaneously. *Dev. Biol.* **425**, 101-108. doi:10.1016/j.ydbio.2017.03.017

van der Wijk, A. E., Wisniewska-Kruk, J., Vogels, I. M. C., van Veen, H. A., Ip, W. F., van der Wel, N. N., van Noorden, C. J. F., Schlingemann, R. O. and Klaassen, I. (2019). Expression patterns of endothelial permeability pathways in the development of the blood-retinal barrier in mice. *FASEB J.* **33**, 5320-5333. doi:10.1096/fj.201801499RRR

Wircer, E., Ben Dor, S. and Levkowitz, G. (2016). Non mammalian models for neurohypophysial peptides. In *Molecular Neuroendocrinology* (ed. D. M.a.H. Gainer). pp. 301-328. Wiley-Blackwell. doi:10.1002/9781118760369.ch14

Wircer, E., Blechman, J., Borodovsky, N., Tsoory, M., Nunes, A. R., Oliveira, R. F. and Levkowitz, G. (2017). Homeodomain protein Otp affects developmental neuropeptide switching in oxytocin neurons associated with a long-term effect on social behavior. *Elife* **6**, e22170. doi:10.7554/eLife.22170

Xie, J., Farage, E., Sugimoto, M. and Anand-Apte, B. (2010). A novel transgenic zebrafish model for blood-brain and blood-retinal barrier development. *BMC Dev. Biol.* **10**, 76-76. doi:10.1186/1471-213X-10-76